Materials Characterization 155 (2019) 109834

Contents lists available at ScienceDirect

Materials Characterization

journal homepage: www.elsevier.com/locate/matchar

Microstructure evolution of the TiB_2/Al composites fabricated by powder metallurgy during hot extrusion

Q. Yang[a], D.L. Cheng[b], J. Liu[a], L. Wang[a], Z. Chen[a,*], M.L. Wang[c], S.Y. Zhong[c], Y. Wu[c], G. Ji[d], H.W. Wang[a]

[a] State Key Laboratory of Metal Matrix Composites, Shanghai Jiao Tong University, Shanghai 200240, PR China
[b] Beijing Institute of Astronautical Systems Engineering, Beijing 100076, PR China
[c] School of Materials Science and Engineering, Shanghai Jiao Tong University, Shanghai 200240, PR China
[d] Unité Matériaux et Transformations, CNRS UMR 8207, Université Lille, Villeneuve d'Ascq 59655, France

ARTICLE INFO

Keywords:
Fine grains
Dynamic recrystallization
Dislocation slip
Grain boundary sliding
TiB_2 particles

ABSTRACT

The microstructure evolution near the central axis during hot extrusion for the fine-grained TiB_2/Al-Zn-Mg-Cu composites fabricated by powder metallurgy is studied by experimental observation at different locations in the remaining die. The significant increase of the fraction of ultrafine grains and texture evolution indicates the extensive dynamic recrystallization at the narrowest position of the die. The deformed grains are distinguished from the undeformed grains with the parameter of grain orientation spread (GOS). And the deformed grains are generally rotated around the extrusion direction. Additionally, the introduced submicron TiB_2 particles have the potential to stimulate the dynamic recrystallization associated with progressively increased misorientation of subgrain boundaries, and even change the spatial distribution of the low angle grain boundaries. The preferential activation of {111} ⟨1 − 10⟩ system and non-octahedral (NOC) slip system {001} ⟨110⟩ contributes to the formation of strong deformation fiber texture according to the analysis of the Schmid factor. It is supposed that grain boundary sliding accommodated dislocation slip mechanism controls the microstructure evolution.

1. Introduction

It has been recognized that the mechanical properties and physical properties of the alloys/composites are greatly influenced by the microstructure of the materials fabricated through the thermo-mechanical process, especially by grain size refinement described by well-known Hall-Petch relationship [1–3]. These different thermo-mechanical processing technologies, such as hot torsion [4], hot rolling [5,6], hot extrusion [7], are greatly studied, generally inducing strong deformation texture. The ratio and type of these possible textures depend on the processing parameters, especially the processing temperature and strain rate. Numerous experimental efforts have been directly devoted to understanding the formation and transformation of deformation textures [4–7]. Furthermore, a number of theoretical models have been reported to successfully simulate the evolution of deformation textures through finite element analysis associated with specified deformation mode and activation slip systems [8,9]. Hot extrusion is one of the most often used hot working processes in the industrial application for lightweight metals. The predominant deformation texture of ⟨111⟩//extrusion direction is often observed which is supposed to facilitate strength enhancement, accompanied with weaker ⟨001⟩//extrusion direction in aluminum alloys [10,11]. However, the development of these fiber textures formed during extrusion is rarely investigated.

In addition to strong deformation textures induced through hot extrusion, coarse grains are also greatly refined, which is attributed to the occurrence of dynamic recrystallization (DRX) [12,13]. The formation of much finer grains compared with original coarse microstructure usually indicates the occurrence of dynamic recrystallization [12]. The DRX mechanisms can be mainly summarized as two types based on the nucleation and growth characteristics: continuous dynamic recrystallization (cDRX) and discontinuous dynamic recrystallization (dDRX) [14]. The new grains form as a result of the increase in sub-boundary misorientation brought about by continuous accumulation of the dislocations introduced by the deformation, which is typical as cDRX [15]. The onset of geometric dynamic recrystallization (GDRX) may be observed with large strain when the separation of prior boundaries approaches the subgrain size [16]. Another mechanism of formation of new grains is that new grains nucleate by grain boundary bulging followed by grain growth and the serrated grain boundaries are often observed, which is typical as discontinuous

* Corresponding authors.
E-mail address: zhe.chen@sjtu.edu.cn (Z. Chen).

https://doi.org/10.1016/j.matchar.2019.109834
Received 24 May 2019; Received in revised form 8 July 2019; Accepted 23 July 2019
Available online 24 July 2019
1044-5803/

dynamic recrystallization (dDRX) [15]. It is well acknowledged that dynamic recrystallization grains often nucleate at the primary grain boundaries due to higher stored energy. Therefore finer primary grain size gives rise to a higher fraction of grain boundaries and leads to DRX [15]. The studies on the effect of introduced ceramic particles on the microstructure evolution during thermo-mechanical process generally conclude that the observations of weaker deformation texture and finer mean grain size result from particles stimulated nucleation mechanism [15,17,18].

However, these studies are generally focused on the coarse-grained materials and based on the dislocation slip mechanism. There is rare research on the microstructure evolution of the fine-grained materials during the thermo-mechanical process. The composites fabricated by powder metallurgy have finer grain size usually smaller than 10 μm. Deformation mechanism maybe transit from dislocation slip control to grain boundary sliding mechanism which is the typical deformation mechanism for ultrafine-grained materials especially deformed under elevated temperature [19–21].

In the present work, the microstructure evolution during hot extrusion of the fine-grained composites fabricated by rapid solidification/powder metallurgy (RS/PM) is investigated using a scanning electron microscope (SEM) with electron back-scattered diffraction (EBSD). Firstly, the microstructures of the composites after spark plasma sintering, at different locations in the remaining die are characterized and analyzed by EBSD. The parameter of grain orientation spread (GOS) is used to distinguish the undeformed grains from deformed grains. Furthermore, the deformation texture is discussed in terms of selection of slip systems under elevated temperature according to the analysis of the Schmid factor.

2. Experimental procedure

The composite powders with pre-embedded nanoscale TiB_2 particles were fabricated by gas atomization. The chemical composition of the composite powders in this study is 10.02 wt% Zn, 2.5 wt% Mg, 2.5 wt% Cu, 4.86 wt% Ti, 2.23 wt% B and balance Al. The atomized powders were directly subjected to spark plasma sintering (SPS) on an FCT H-HP D 25 system. The sintering experiments were conducted at the temperature of 480 °C and under uniaxial loading of 50 MPa for 5 min in a graphite mold with an inner diameter of 40 mm. The heating rate was about 100 °C/min, the standard 12:2 pulse sequence was adopted. The sintered compacts were in diameter of 40 mm and height 40 mm. The compacts were machined into billets with a diameter of 39.5 mm and put in the steel mold heating in the electrical resistance furnace to 723 K. The billet was extruded with an extrusion ratio of 16 under a ramp speed of 0.8 mm/s. Fig. 1a shows the schematic illustration of the extrusion setup used in the present study.

The microstructure of the composites was studied by electron back-scattered diffraction (EBSD). The observed positions were illustrated in Fig. 1b including position A, B, C, D, E and F. The position A represents the materials after SPS without extrusion, position B, C, D, and E are located within material remaining in the extrusion die, whereas position F was completely extruded. The different positions represent different equivalent strain that the materials have undergone during extrusion. There is an empirical expression evaluating the equivalent strain at each position according to the corresponding extrusion ratio:

$$\varepsilon = \ln(B) \quad (1)$$

The true strain that the composites underwent at each position is calculated according to the above expression as shown in Fig. 1c. The material remaining in the die was spark machined along the extrusion center axis and then polished with increasingly finer emery paper. After a finial emery paper with 3 μm diamond powder, the material was then polished with 1.5 and 0.5 μm diamond colloidal solution. Finally, the material was polished by Leica EM TIC 3× for 1.5 h. Thereafter, the microstructure was characterized by TESCAN MAIA3 scanning electron microscope (SEM) and equipped BRUKER e-FlashHR electron back-scattered diffraction (EBSD) detector. For comparison, the extruded microstructure of the alloy under the same extrusion condition is also characterized by EBSD, and the microstructures of materials remaining in the die are not observed.

3. Results

Fig. 2 gives the IPF maps of the composites at different positions shown in Fig. 1b. The X direction is perpendicular to the compression direction at location A on the sintered sample and parallel to the extrusion direction (ED) at other locations. The thick black lines represent the high angle grain boundaries ($\theta > 15°$) and thin green lines represent the low angle grain boundaries ($2° < \theta < 15°$). The TiB_2 particles are in black spots. In Fig. 2a, some subgrains are observed whereas most of the grains are not deformed with a small fraction of low angle grain boundaries. In Fig. 2b, grains are deformed along the direction perpendicular to ED. With further deformation, the deviation angle between ED and grains deformation direction tends to decrease as shown in Fig. 2c, d. The IPF images at the position of E and F show that the grains are elongated along ED. Fig. 3 shows the measured deviation angle between ED and grains deformation direction at each position. The deviation angle gradually decreases to 0° with increasing strain.

Fig. 4 displays the inverse pole figures (IPFs) from EBSD analysis at each position. Fig. 4a and b show the IPFs at the location of A and B exhibiting the weak ⟨101⟩//Y0 direction texture. The Y0 direction is parallel to the compression direction during SPS at location A and perpendicular to ED at other locations during extrusion. Due to the axisymmetric process of the extrusion, the Y0 and Z0 direction are interchangeable at the EBSD pattern on the extruded sample. However, at location B, the equivalent true strain is low and the samples may undergo further compressive strain due to the little smaller diameter of the compact than the inner diameter of the extrusion mold, it is supposed that the grains are deformed along Y0 direction which is perpendicular to ED for consistency. The maximum IPF intensity is increased from 1.31 at position A to 2.36 at position B. The IPFs at location C and D exhibit the weak ⟨101⟩//Z0 direction. However, the maximum IPF intensity is identical in two positions. With further deformation, the microstructures exhibit the ⟨111⟩//X0 direction at position E and F as shown in Fig. 4e and f. The X0 direction is along the extrusion direction. The maximum intensity increases from 4.66 at position E to 7.36 at position F. In addition to the formation of ⟨111⟩ fiber texture at position F, the microstructure exhibits weak ⟨001⟩ fiber texture along the ED.

Fig. 5 shows the evolution of fraction of ⟨001⟩ and ⟨111⟩ fiber texture at each position. The maximum deviation angle of 15° is adopted. The volume fraction of ⟨001⟩ and ⟨111⟩ fiber texture after spark plasma sintering is minimum. With increasing deformation, the volume fractions of these deformation textures increase generally. However, there is a little change at position of B, C and D. The volume fraction of ⟨111⟩ fiber texture at position E increases rapidly to 37.8% from 15.7% at position D and fraction of ⟨100⟩ fiber texture is comparable to that at the position D. After complete extrusion, the volume fraction of ⟨111⟩ fiber texture at position F is comparable to that at position E and the volume fraction of ⟨100⟩ fiber texture is increased steeply from 16.4% at position E to 30.8% at position F.

Fig. 6 analyzes the evolution of the fraction of low angle grain boundaries (LAGBs), mean LAGBs and mean high angle grain boundaries (HAGBs) during extrusion at each position. The mean LAGBs (HAGBs) is defined as the sum of misorientation of LAGBs (HAGBs) multiplied by the according volume fraction. The formation of LAGBs results from rearrangement of dislocations produced during extrusion. The deformation strain during spark plasma sintering is small and the volume fraction of LAGBs is lowest. In general, the mean LAGBs and fraction of LAGBs increase until at position E as a result of increased equivalent strain, despite that the mean HAGBs have the opposite trend.

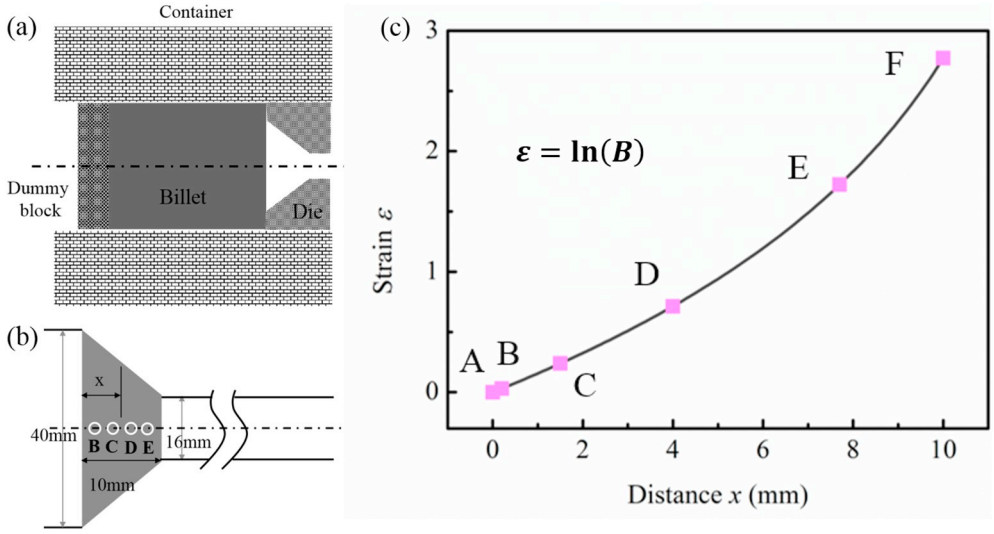

Fig. 1. (a) The schematic illustration of the extrusion setup; (b) the selected observed locations in the remaining die; (c) the corresponding strain at each selected position.

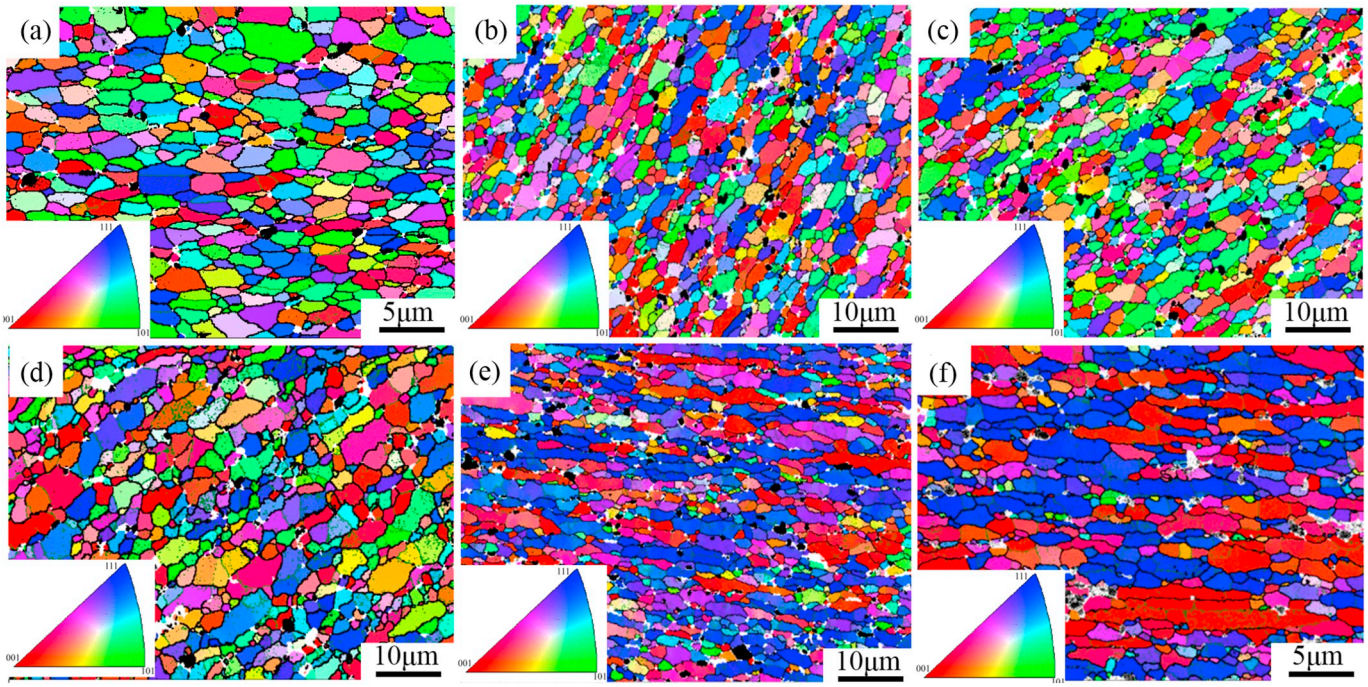

Fig. 2. The inverse pole figures (IPF) at each position. The high angle grain boundaries (HAGBs) with $\theta > 15^{\circ}$ are in thick black line; the low angle grain boundaries (LAGBs) are in thin green lines. (For interpretation of the references to colour in this figure legend, the reader is referred to the web version of this article.)

However, there is a decrease in the fraction of LAGBs and mean LAGBs at location F. This may result from the occurrence of post-DRX since no timely quench can be performed for extrusion direction. The microstructures produced by DRX are unstable at elevated temperature. The new dislocation-free grains involving the rearrangement of dislocations produced during extrusion may nucleate and grow further.

Fig. 7 indicates the evolution of the average grain size and the fraction of the ultrafine grains at each position. Although the average grain size shows no large variation, the mean grain size decreases with increasing equivalent strain. The grain size steeply increases when the compact is completely extruded at location F. This may result from grain growth due to the longer duration at the elevated temperature after extrusion since no timely quench. The fraction of ultrafine grains steeply increases to 22% at position E and the average grain size at position E is finest. The steep increase of these ultrafine grains usually results from the occurrence of dynamic recrystallization. It means that the dynamic recrystallization greatly occurs at position E.

One parameter which has been employed to distinguish the deformed grains from the undeformed grains is the grain orientation spread (GOS). GOS of grain i is expressed as:

$$GOS(i) = \frac{1}{J(i)} \sum_{j} w_{ij} \tag{2}$$

where $J(i)$ is the number of pixels in grain i, w_{ij} is the misorientation angle between the average orientation of grain i and the orientation of pixel j. During hot deformation, the deformed grains have a high value of GOS, and the recrystallized grains or undeformed grains possess the low value of the GOS. The parameter of GOS has been used to investigate the dynamic recrystallization of Al alloy, Mg alloys and other

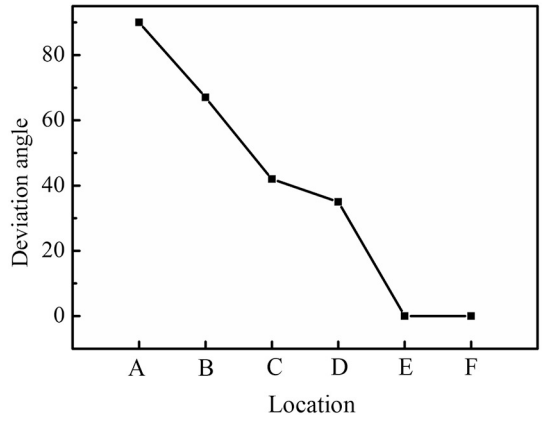

Fig. 3. The deviation angle between extrusion direction and grain deformation direction at each position.

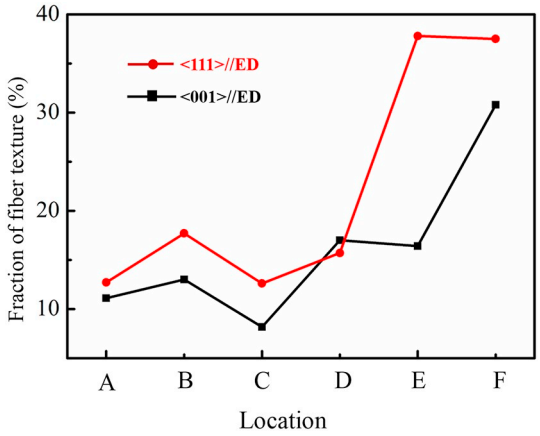

Fig. 5. The fraction of ⟨111⟩ and ⟨001⟩ fiber texture evolution at each position.

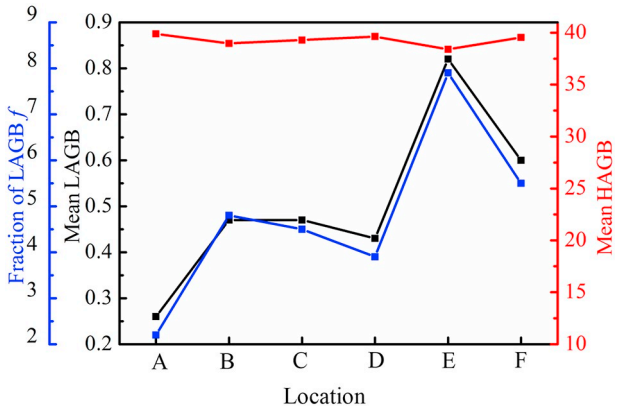

Fig. 6. The mean LAGBs in black line and dots, mean HAGBs in red line and dots, and the fraction of LAGBs in blue line and dots at each position. (For interpretation of the references to colour in this figure legend, the reader is referred to the web version of this article.)

alloys under hot working [22,23]. Fig. 8 shows the EBSD IPF maps of components at position E (a) with GOS > 1°; (b) with GOS > 1° and ⟨111⟩ fiber texture; (c) with GOS > 1° and ⟨100⟩ fiber texture; (d) with GOS < 1°. The component of grains with GOS > 1° consists of deformed grains, and the component of grains with GOS < 1° consists of recrystallized grains and boundary sliding grains. Fig. 8e–h give the corresponding misorientation axes distribution in the sample coordinate, X and Y direction represent ED and radial direction respectively. It is observed that the maximum density of misorientation axes for deformed grains occurs near the ED in Fig. 8e. However, the crystallographic direction of the ED cannot be determined. For the component of deformed grains with ⟨111⟩ fiber texture, the misorientation axes distribution is more concentrated around ED as shown in Fig. 8f. For the component of grains with ⟨001⟩ fiber texture, the misorientation axes distribution occurs around ED. However, the distribution is comparatively diffuse. The distribution of the misorientation axes for the undeformed/recrystallized grains is random. Fig. 8i–l show the misorientation axes distribution in the crystal coordinates. For deformed grains, the misorientation axes distribute along the direction in the (10−1) plane and mainly focuses around ⟨101⟩ and ⟨111⟩ direction. As for the component of grains with ⟨111⟩ fiber direction, the misorientation axes focus in the vicinity of ⟨111⟩ direction, there is, however, a spread away from ⟨111⟩ direction to the closest ⟨112⟩ direction in Fig. 8j. Rotation axis of ⟨112⟩ is the Taylor axis of slip system of (11−1) ⟨1−10⟩. In Fig. 8k, the misorientation axes are distributed along different directions encompassing ⟨101⟩ and ⟨112⟩ direction. Rotation axis of ⟨101⟩ is the Taylor axis of slip system of (001) ⟨10−1⟩. For the component of grains with GOS < 1°, the misorientation axes distribute rather randomly and no obvious concentrated intensity could be observed which is similar to the result obtained from the misorientation axes in the sample coordinates. Fig. 8m–p display the corresponding misorientation angle distribution. The percentage of LAGBs is 7.9%, 16.4%, 41.9% and 3.2% respectively for four components. Both grain boundary sliding (GBS) mechanism and dynamic recrystallization behavior contribute to the lowest fraction of LAGBs.

Although the parameter of GOS has been employed to distinguish the undeformed grains from deformed grains, it is difficult to distinguish the recrystallized grains and boundary sliding grains through this parameter. There are many studies on the orientation of recrystallized grains with deformed matrix and found that the recrystallized grains have a 40°⟨111⟩ relationship to the deformed matrix [24,25]. Dryzymala et al. [26] investigated recrystallization behavior in stable aluminum-base single crystals and found that there were 7 classes of misorientation axes including ⟨001⟩, ⟨011⟩, ⟨012⟩, ⟨111⟩, ⟨112⟩, ⟨122⟩ and ⟨123⟩ low-index directions. Near ⟨111⟩ axes was not the single main misorientation axes, axes belong to the neighborhood of ⟨221⟩ and ⟨012⟩ directions and to a lesser degree of ⟨112⟩ were often highly represented. In the present work, Fig. 9 shows three typical orientation of grains with GOS < 1° to the neighboring deformed matrix

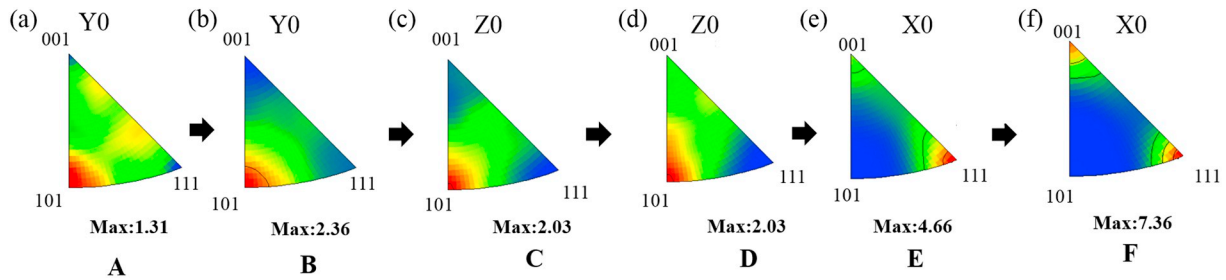

Fig. 4. Inverse pole figures generated from EBSD analysis at each position. And the maximum intensity is also indicated.

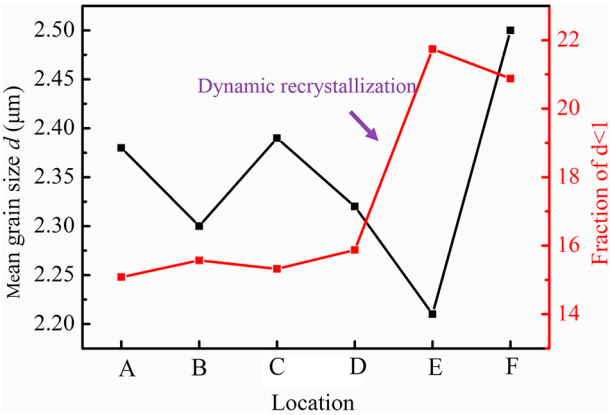

Fig. 7. The variation of the mean grain size and a fraction of ultrafine grains.

at position E. Fig. 9a shows the IPF map of grain cluster 1. The grain A has a GOS < 1° and grain B has been deformed with several small angle grain boundaries. The misorientation axis distribution in the sample coordinates is displayed in Fig. 9b. It is observed that the orientation of grain A is linked to the orientation of grain B by rotation around misorientation axes as marked by the red point T1. Fig. 9c gives this rotated crystallographic axis as ⟨102⟩ axes. Fig. 9d gives another IPF map of grain cluster 2. As analyzed above, the orientation of grain C is linked to the orientation of grain D by rotation around crystallographic ⟨112⟩ axes. Fig. 9g shows another IPF maps of grain cluster 3. The orientation of grain E is rotated around a crystallographic axis as ⟨101⟩ axes. Therefore, the special orientation of grain A, C and E to the neighboring deformed matrix makes it reasonable to assume that the grains A, C and E are recrystallized grains.

Fig. 10a shows the EBSD quality pattern at position E. The TiB_2 particles are in black spots. The HAGBs are in thick black lines, the LAGBs with 5° < θ < 10° are in red lines and the LAGBs with 10° < θ < 15° are in green line. Most of the identified TiB_2 particles are located at grain boundaries whereas there are also some particles distributed within grains. The LAGBs without interaction with TiB_2 particles are usually perpendicular to ED. The presence of TiB_2 particles within grains influences the spatial distribution of LAGBs. Fig. 10b–d give three typical grains in which TiB_2 particles interact with LAGBs. The LAGBs around TiB_2 particles lie parallel or inclined to the ED and LAGBSs away from TiB_2 particles are perpendicular to the ED. Fig. 10e gives the IPF map of one grain without identified TiB_2 particles. It is observed that the LAGBs are perpendicular to the ED.

Fig. 11a displays the IPF map of deformed grain A with several subgrains. The LAGBs with 5° < θ < 10° are in thick red lines and LAGBs with 10° < θ < 15° are in thick yellow lines. The grain A shows the orientation with ⟨111⟩ crystallographic axis nearly parallel to ED. Most of the subgrains have misorientation angle in the range of 5°–10° in red lines. However, there is a subgrain A1 with a misorientation angle larger than 10°. This subgrain has a comparatively different orientation with ⟨101⟩ crystallographic axes nearly parallel to ED. Fig. 11b gives the misorientation line scan along the red arrow direction. The misorientation steeply increases at the subgrain boundary. Therefore, the subgrain is assumed as the dynamic recrystallization nucleus. Fig. 11c exhibits the IPF map of deformed grain B and recrystallized grain C. Fig. 11d gives the typical misorientation line scan along the red arrow direction marked in Fig. 11c. The orientation of the recrystallized grain C is similar to that of the subgrain A1 in Fig. 11a, and the orientation of deformed grain B is similar to the orientation of grain A. The misorientation between the deformed grain B and recrystallized grain C reaches 32°. Therefore, the grain C is assumed to be progressively continuous dynamic recrystallized grain from the deformed matrix B. Fig. 11e gives the IPF maps of grain D and there is one TiB_2 particle located within grain D. And Fig. 11f shows the misorientation line scan along the red arrow. The introduction of TiB_2 particle leads to the formation of subgrain D1 with larger misorientation of 11°. The subgrain D1 is assumed as the particle stimulated recrystallized nucleus. Fig. 9g shows another IPF map of grain E and grain F. The TiB_2 particle is located at grain boundary between F and E. And the misorientation between grain F and grain E reaches to 38°. The TiB_2 particle has successfully simulated dynamic recrystallization. In addition, the EBSD pattern of the extruded alloy without TiB_2 particles

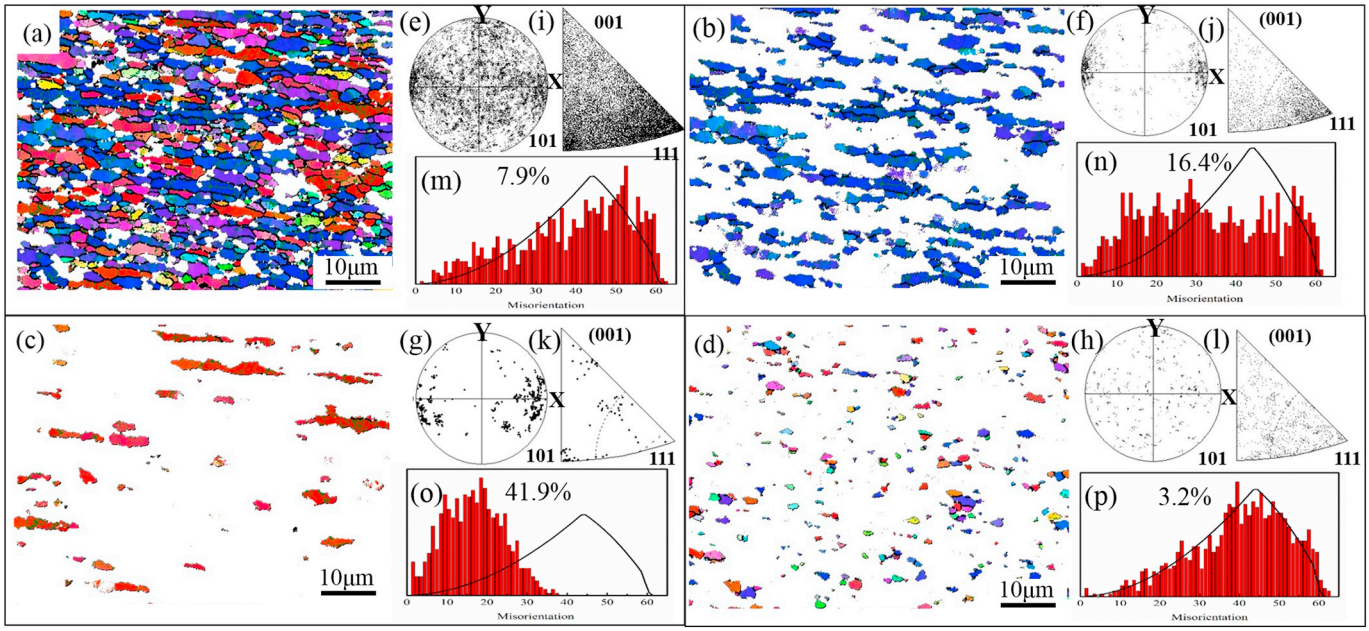

Fig. 8. The inverse pole figure (IPF) maps of the grains with (a) grain orientation spread (GOS) > 1°; (b) GOS > 1° and ⟨111⟩ fiber texture with maximum deviation angle of 15°; (c) GOS > 1° and ⟨100⟩ fiber texture with maximum deviation angle of 15°; (d) GOS < 1°. (e)–(h) are the misorientation axes in the sample coordinates for the component in (a)–(d), respectively. The X direction represents the extrusion direction and Y direction represents the radial direction. (i)–(l) are the misorientation axes in the crystal coordinates for the grains component in (a)–(d), respectively. (m)–(q) are the faction of low angle grain boundaries (LAGBs) for the grains component in (a)–(d), respectively.

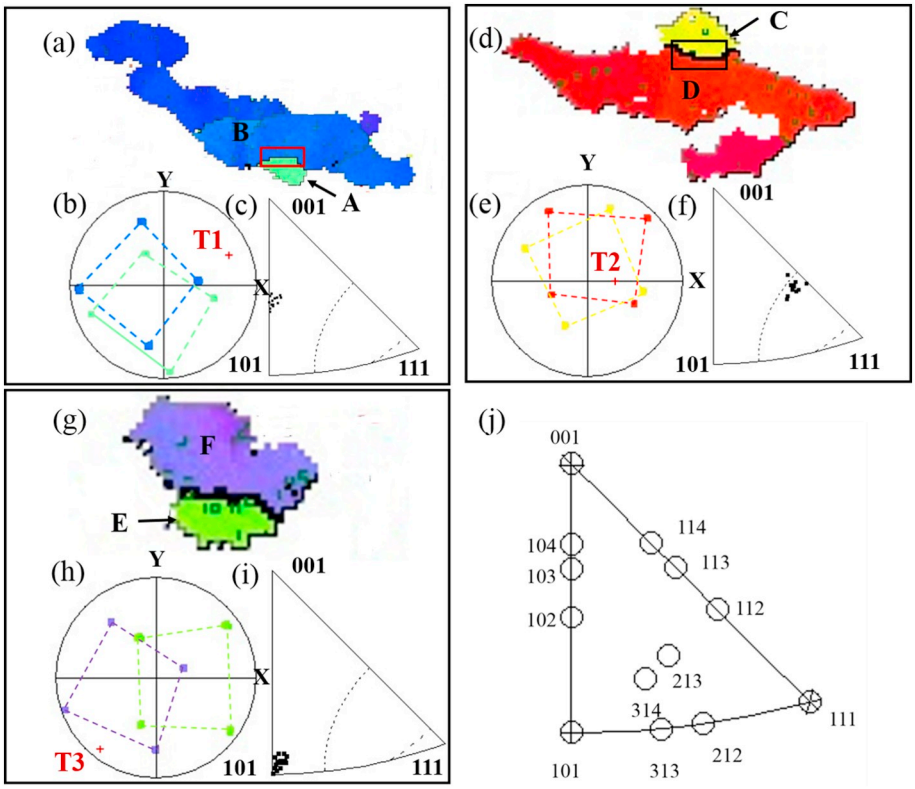

Fig. 9. (a) (d) (g) Typical inverse pole figure (IPF) maps of three grain clusters with one recrystallized grain neighbored to the deformed matrix. (b) (e) (h) The misorientation axes in the sample coordinates showing a rotation of recrystallized grain around different axes. (c) (f) (i) The misorientation axes in the crystal coordinates showing the rotation axis along the crystallographic axes respectively.

under the same extrusion condition is given in Fig. 12a. The average grain size about 3.12 μm in Fig. 12b is larger than the final average grain size of extruded composites at location F. Additionally, the aspect ratio of the extruded alloy is larger. Therefore, the TiB_2 particles in the present work have stimulated dynamic recrystallization.

From the bright-field transmission electron microscope (TEM) images in Fig. 13a–c, the interaction of dislocations produced during extrusion with second phases including TiB_2 particles, interphases and Al_3Zr can be observed. The accumulation of dislocations around the second phases constitutes the driving force for dynamic recovery and dynamic recrystallization. A critical particle size should be reached to provide enough driving force to trigger particle stimulate nucleation (PSN), which was reported by Humphreys et al. [27], McNelley et al. [16] and Huang et al. [28]. And it is concluded that the critical size for PSN decreases with increasing strain, and PSN occurs at particles > 1 μm typically [28]. A smaller critical particle size about 0.68 μm was also found in the annealed Fe-0.4C alloy. In the present work, the TiB_2 particles size are in the range of 25–500 nm with a mean average size of 100 nm according to our previous study [29]. The TiB_2 particles are too fine to stimulate the dynamic recrystallization nucleation under the processing condition in the present work. However, the critical particle size model should take the particle clusters and fine grain size into consideration. Although the TiB_2 particles are uniformly distributed in the matrix, there are also some TiB_2 particles in clusters at local regions as shown in red arrows in Fig. 10a. These local TiB_2 particles clusters have the potential to stimulate dynamic recrystallization behavior. This effect was also reported in Ref. [30] that second-phases particle clusters in AA3104 aluminum alloy were very powerful preferential recrystallization nucleation sites. In addition to particle clusters, the large fraction of grain boundaries with more stored energy can improve the ability for particles to stimulate the dynamic recrystallization behavior. Relatively obvious dislocation walls can be observed in Fig. 13d–f, showing the typical characteristic of dynamic recovery and recrystallization.

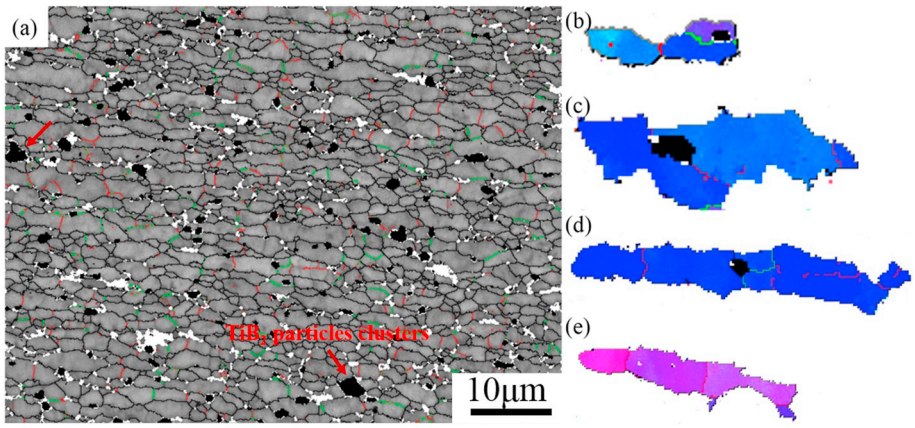

Fig. 10. (a) shows the EBSD quality map at position E. The low angle grain boundaries (LAGBs) with misorientation $5^\circ < \theta < 10^\circ$ are shown in red lines, with misorientation $10^\circ < \theta < 15^\circ$ in green lines and the high angle grain boundaries (HAGBs) with misorientation $\theta > 15^\circ$ in thick black lines. The TiB_2 particles are shown in black spots. (b)–(d) give three typical examples showing the interaction of subgrain boundaries with a TiB_2 particle located within the grain. (For interpretation of the references to colour in this figure, the reader is referred to the web version of this article.)

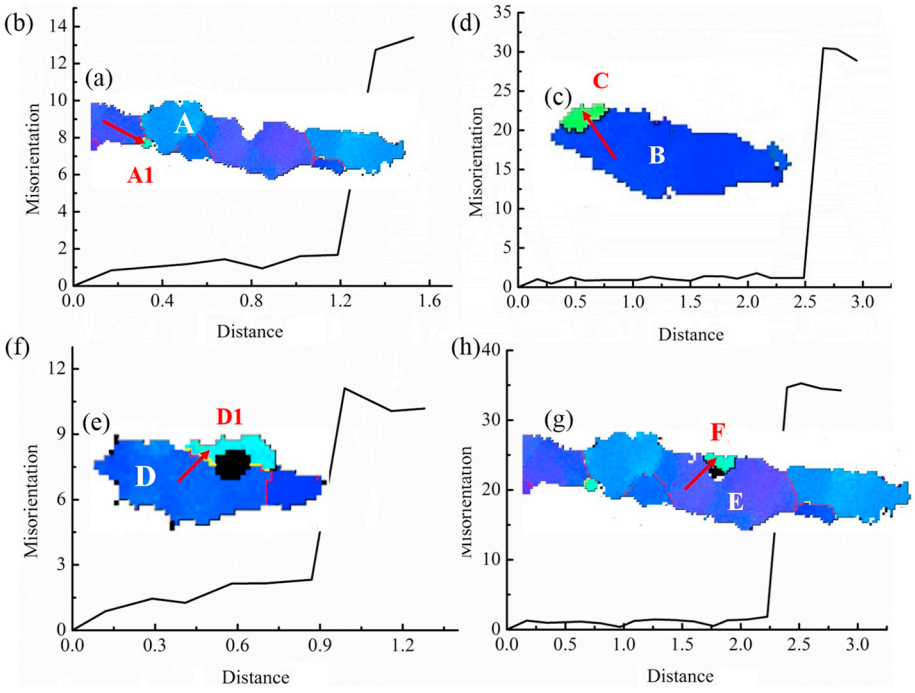

Fig. 11. (a) (c) show the inverse pole figure (IPF) maps of single grain or two grains without TiB_2 particles, (e) (g) show the inverse pole figure maps of single grain or two grains with TiB_2 particle. (b) (d) (f) (g) give the misorientation line scan along the red arrow marked in (a) (c) (e) (g). (For interpretation of the references to colour in this figure, the reader is referred to the web version of this article.)

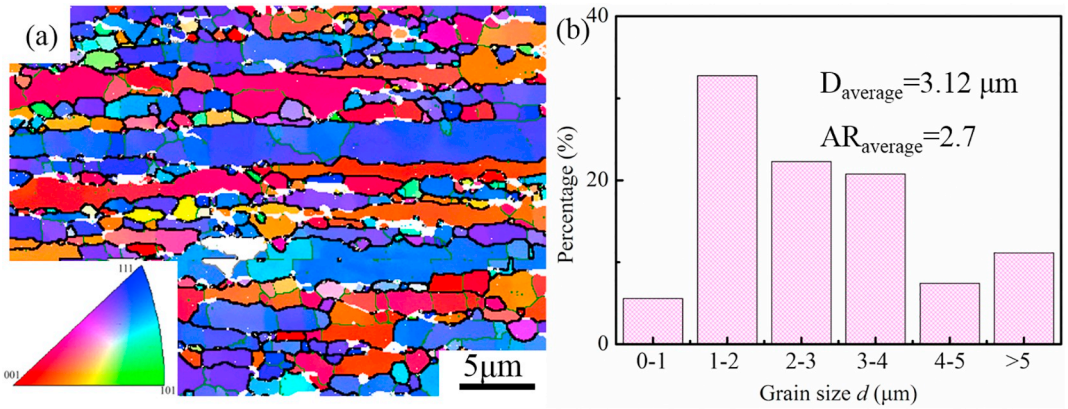

Fig. 12. (a) IPF map of the extruded alloy; (b) the size distribution of the extruded alloy, average grain size and aspect ratio are given in the inset.

4. Discussion

4.1. The formation of deformation texture

Mayama et al. [31] have modeled the full extrusion process of magnesium alloy by finite element analysis, and calculated the strain components ε_{xx}, ε_{zx}, ε_{yy} at three positions along the radial direction from a central point to the periphery in the plane perpendicular to the extrusion direction. And it was found that the shear strain ε_{zx} near the central axis is negligibly small to the normal strain, while ε_{zx} at the peripheral position is comparable to the normal strain. It was concluded that the deformation near the central axis of the extruded rods is well approximated by equi-biaxial compressive straining. The volume elements are predominated by normal stress. It was well acknowledged that the formation of deformation texture is dominated by the activated slip system [32–34]. When the resolved shear stress along the slip direction on the slip plane reaches the critical resolved shear stress (CRSS), the slip system is activated. The {111} ⟨110⟩ slip system is well acknowledged to be predominated during deformation at room temperature in aluminum alloys. The microstructure and local crystallography in aluminum alloys during deformation were systematically studied [26,35]. However, at elevated temperature, in addition to the usual {111} ⟨110⟩ slip system, non-octahedral (NOC) slip systems are also possible to be activated including {110} ⟨110⟩, {112} ⟨110⟩ and {100} ⟨110⟩ [36]. Maurice and Driver et al. [37] have analyzed the activation of slip systems during high-temperature plane strain compression of aluminum crystals. It was concluded that at low temperature regime, the slip system was dominated by {111} ⟨110⟩, at intermediate temperature {111} and {110} ⟨110⟩ slip systems occurred concurrently and at high temperature the {110} ⟨100⟩ slip was dominated. It was pointed out that maybe the {100} ⟨110⟩ family is most significant contribution apart from {111} ⟨110⟩ slip system, because the {100} planes are the most densely packed after {111} planes.

The selection of the activated slip systems depends on the resolved shear stress $\boldsymbol{\tau_\alpha}$ along the slip direction and the critical resolved shear stress (CRSS). The relation between the applied stress $\boldsymbol{\sigma}$ and $\boldsymbol{\tau_\alpha}$ on a given slip system can be written using the Schmid factor $\boldsymbol{S}$ as

$$\tau^{\alpha} = \sigma^{*}S \tag{3}$$

$$S = S^{\alpha} \times \mathrm{n}^{\alpha} \tag{4}$$

where $\boldsymbol{S^\alpha}$ is the slip direction vector, $\boldsymbol{n^\alpha}$ is the slip plane normal direction vector. If $\boldsymbol{\tau_\alpha}$ is larger than CRSS, the slip system is activated. However, CRSS of the different slip system at elevated temperature is lack, and most studies assumed the strength of different slip system to

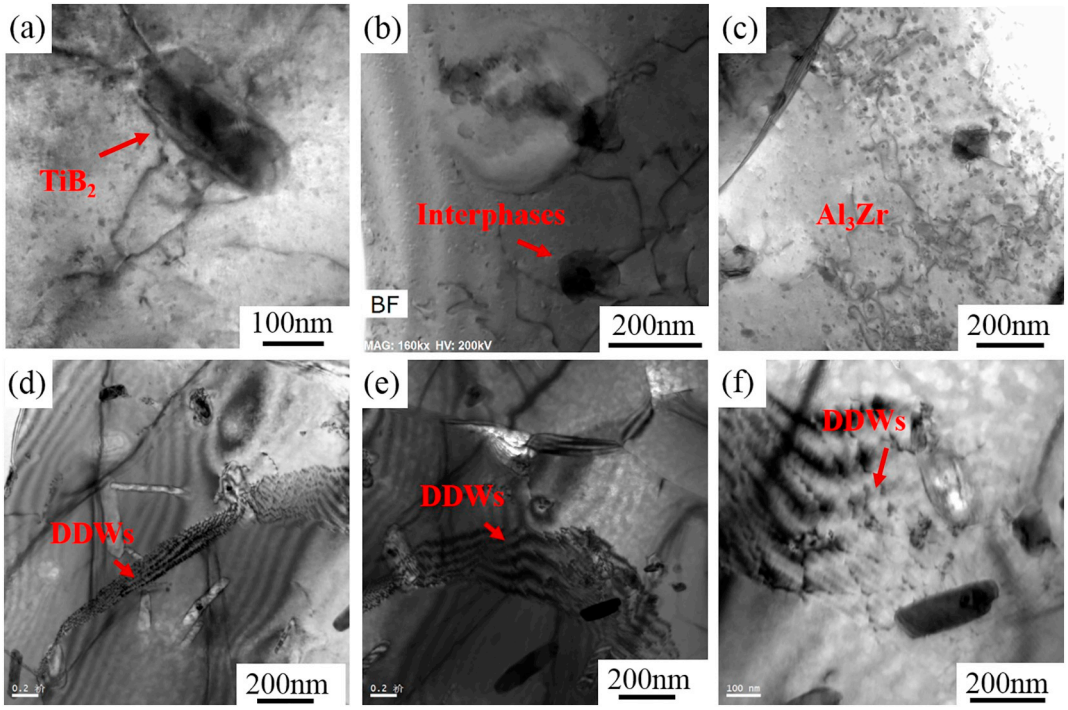

Fig. 13. Bright-field transmission electron microscope (TEM) images of extruded samples.

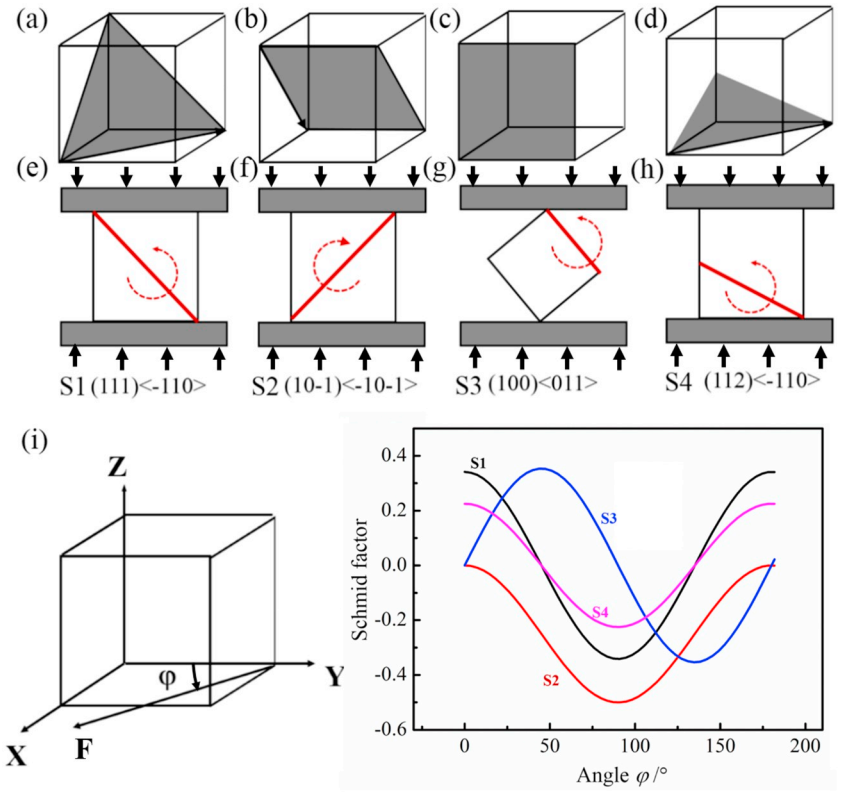

Fig. 14. Illustration of schematic view of the (a) S1 slip system; (b) S2 slip system; (c) S3 slip system; (d) S4 slip system; (e) rotation of S1; (f) rotation of S2; (g) rotation of S3; (h) rotation of S4; (i) schematic view of applied load direction; (j) the calculated Schmid factor of four slip systems vs. applied load direction angle φ.

be the same. Fig. 14 illustrates the schematic view of slip system of (a) **S1** (111) [−110] (b) **S2** (10–1) [−10−1] (c) **S3** (100) [011] and (d) **S4** (112) [−110], respectively. Fig. 14i shows a schematic diagram of the loading direction ***F*** and the angle φ. Fig. 14j shows the relation between the calculated Schmid factor S of four slip systems and the angle φ. It is observed that the Schmid factor of the **S1** slip system and **S3** slip system predominate over the **S2** and **S4** slip systems. Therefore, resolved shear stress on the **S1** and **S3** slip systems is larger than that on the other two slip systems. During hot extrusion, if it is assumed that CRSS of the different slip systems is identical, the **S1** and **S3** slip system will be

Table 1
The Taylor axis of the four possible slip systems.

Slip system	S1	S2	S3	S4
Taylor axis	⟨11 − 2⟩	⟨010⟩	⟨01 − 1⟩	⟨11 − 1⟩

preferentially activated in the materials along the extrusion axis. The activation of the slip system not only depends on the Schmid factor but also depends on the internal stress state of the volume elements. As for the case of extrusion into rods, the normal stress ε_{xx} and ε_{yy} are identical along the rod axis. The preferential activation of **S1** and **S3** slip systems may be not applicable for the other cases like extrusion into plates or hot rolling because the internal stress state of volume elements is not symmetric. During hot rolling or ECAP, the complexity of the stress distribution on the volume elements makes it more complex to predict activation of the slip system.

According to the Taylor model, the slip plane and slip direction of the activated slip system would rotate along the Taylor axis. The Taylor axis is defined as:

$$T = S \times n \tag{5}$$

The Taylor axis lies on the slip plane and perpendicular to the slip direction. The Taylor axis of the four possible slip systems at elevated temperature is summarized in Table 1. Fig. 14e, f, g and h show the schematic illustration of the rotation of the slip plane along the Taylor axis.

Next, the development mechanism of the fiber texture during hot extrusion for aluminum alloy is discussed. It is specified to clarify the reason why the normal directions of the {111} planes and {100} planes, rather than that of the {110} planes, are parallel to the extrusion direction. We first consider the ⟨111⟩ fiber texture. As discussed above, the condition of applied stress on the {001} planes is taken into consideration. The three equivalent slip systems including **S1** (1 1 1) [−1 0 1], **S5** (1 −1 1) [1 1 0] and **S6** (−1 −1 1) [1 −1 0] are into consideration. Fig. 15 shows the Schmid factor between the applied stress and the three slip systems. It is observed that only when the applied stress is parallel to the slip direction (φ = 45°, 135°), the Schmid factors of the three equivalent slip systems are identical, therefore, the three slip systems can be activated simultaneously. In the range of 0° < φ < 45° and 135° < φ < 180°, the Schmid factor of S6 is highest. And in the range of 45° < φ < 135°, the Schmid factor of S5 is highest. Therefore, the single slip will occur unless the applied stress coincides with ⟨110⟩ direction. In the material flow during hot extrusion, more than one slip system must occur simultaneously. Therefore, lattice rotation will occur to make the applied stress coincide with ⟨110⟩ direction and stops at the φ = 45° and 135°. In the case of extrusion, the alignment of the ⟨110⟩ direction along compressive stress

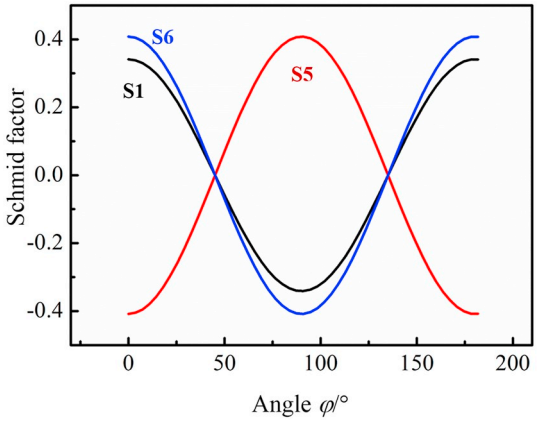

Fig. 15. The relation between each slip system and angle φ.

direction gives rise to the alignment of ⟨111⟩ direction parallel with extrusion direction, and the ⟨111⟩ fiber texture is eventually formed. The formation of ⟨100⟩ fiber texture can be analyzed in the same way.

4.2. Grain boundary sliding accommodated dislocation slip

In addition to the predominated deformation mechanism of dislocation slip, the grain boundary sliding (GBS) also contributes to the microstructure evolution during hot deformation. The mechanism of GBS has been extensively investigated especially in the field of superplastic behavior and creep behavior of polycrystalline materials [38–40]. In general, GBS tends to predominate in fine-grained materials at elevated temperature under low strain rate condition. Perez-Prado et al. [41] have investigated the transition from slip to grain boundary sliding in a discontinuously recrystallized superplastic aluminum alloy, and found that grain boundary sliding occurred when the stress component is in a value smaller than 2 and modulus compensated stress, σ/E, decreases below about 6×10^{-4}. However, it is hard to relate the ramp pressure during extrusion to tensile flow stress. The phenomena of high strain rate superplasticity (HSRS) in the range of 10^{-1}–$50\,s^{-1}$ have been found in the ultrafine-grained aluminum alloys fabricated by powder metallurgy [42]. Mishra et al. [42] have listed the reported high strain rate superplasticity behavior for rapidly solidified aluminum alloys. For example, 2124–0.6Zr alloys fabricated by powder metallurgy with grain size of 1 μm have a total elongation of 500% tested at strain rate of $0.3\,s^{-1}$ in the temperature range of 698 K–773 K, 7075–0.7Zr alloys fabricated by PM have a total elongation of 1000% tested at the strain rate of $0.1\,s^{-1}$ under the temperature of 698 K–823 K. It was reported, that under GBS control of deformation random grain rotations would result in a predominant random texture after deformation, while under dislocations slip control of deformation grains rotation around a specific axis would result in specific deformation texture. During the process of hot extrusion, there is a relationship to estimate the mean strain rate applicable to a conical die with semi-angle as [43]:

$$\dot{\varepsilon_m} = \frac{6Vd_b^2 ln(B)\, tan\,\Phi}{d_b^3 - d_e^3} \tag{6}$$

where V is the extrusion speed in m/s, d_b and d_e are the diameter of billet and extrudate respectively, B is the extrusion ratio, Φ is the semi-angle. In the present work, the average strain rate is estimated to be $0.34\,s^{-1}$. It should be noted that there is a spread of strain rate away from the mean strain rate in the billet during extrusion. However, the mean strain rate is very useful for analysis. Additionally, in the present work, the average grain size after spark plasma sintering is approximately 2.3 μm and there is about a number fraction of 20% grains with a size smaller than 1 μm. The extrusion temperature is 723 K. Therefore, the GBS mechanism is possible to predominate in the ultrafine grains under this processing condition.

According to the observation of the microstructure evolution, there is always a faction of undistorted grains with GOS < 1° at each position and these grains are usually in ultrafine size. The ultrafine grains are usually assumed as recrystallized grains during hot working for castings. It is not applicable in the present case. The fraction of ultrafine grains has changed little at position A, B, C, D and steeply increased at position E. The significant extrusion texture has been formed at position E and the deformed direction of grains is parallel to the extrusion direction. Therefore, it is reasonable to assume that significant dynamic recrystallization occurred at strain between position D and E. There are several phenomenological and theoretical models for hot working and dynamic recrystallization [44] including the better accepted critical strain model [45,46] and critical dislocation density model [47]. The onset of nucleation of DRX is usually associated with the accumulation of dislocations. The total dislocation density including dislocations within cells and within cell walls increases with the increment of strain

level. When the dislocation density in the deformed matrix reaches a critical value, the nuclei for DRX will form on primitive grain boundaries. The dislocations density evolution during the thermomechanical process is described by one parameter model (KM model) and multiple parameter model (MPM) mode [48]. At position B, C and D, the dislocation slip behavior preferentially occurs at larger grains with the formation of LAGBs and there is a large grain orientation spread (GOS) value. However, there is no grain orientation spread (GOS) in the grain with ultrafine size. These grains are assumed to be predominated by grain boundary sliding. Therefore, it is reasonable to assume the GBS mechanism accommodated dislocation slip deformation mechanism is responsible for the microstructure evolution during hot extrusion for in-situ TiB_2/Al-Zn-Mg-Cu composites fabricated by powder metallurgy, although it is difficult to distinguish the recrystallized grains and grain boundary sliding grains in the EBSD analysis.

The extensive occurrence of dynamic recrystallization at position E does not mean that DRX is impossible to occur at position A, B, C and D. A low fraction of subgrain boundaries with misorientation larger than 10° is formed at position A, B, C and D. Wither further deformation, the misorientation will continue to increase. Additionally, the addition of TiB_2 particles could enhance the accumulation of dislocations and increase the misorientation of subgrain boundaries. Therefore, in spite of the substantial occurrence of DRX at position E, it is also possible to occur at position A, B, C and D in the local region with high stored energy due to deformation inhomogeneity.

5. Conclusion

In this study, the microstructure evolution during hot extrusion for fine-grained in-situ TiB_2/Al-Zn-Mg-Cu composites was investigated by EBSD analysis along the extrusion axis. The substantial occurrence of dynamic recrystallization is found at the narrowest position of the die. The parameter of GOS has been employed to distinguish the deformed grains from the undeformed grains. Consequently, the following conclusions are obtained.

1. The grain boundary sliding accommodated dislocation slip mechanism dominates the deformation mechanism and governs the microstructure evolution.
2. The formation of strong ⟨111⟩ and ⟨100⟩ fiber texture results from the preferential activation of {111} ⟨1–10⟩ and non-octahedral (NOC) slip systems {001} ⟨110⟩ at elevated temperature.
3. The deformed grains are related to rotation around ED in the sample coordinates, the grains exhibiting ⟨111⟩//ED orientation are linked to rotation around the crystallographic direction of ⟨111⟩, and the grains displaying ⟨100⟩//ED orientation are linked to rotation around ⟨101⟩ and ⟨112⟩.
4. The submicron TiB_2 particles in the fine-grained composites can also stimulate the initiation of dynamic recrystallization behavior and change the spatial distribution of subgrain boundaries.

Declaration of Competing Interest

No potential conflict of interest was reported by the authors.

Acknowledgment

This work is financially supported by the National Key Research and Development Program of China (Grant No. 2016YFB1100103); the Conseil Regional du Nord-Pas de Calais and the European Regional Development Fund (ERDF).

References

[1] J.R. Zuo, L.G. Hou, J.T. Shi, H. Cui, L.Z. Zhuang, J.S. Zhang, Enhanced plasticity and corrosion resistance of high strength Al-Zn-Mg-Cu alloy processed by an improved thermochemical processing, J. Alloys. Comp. 716 (2017) 220–230.
[2] W.T. Huo, J.T. Shi, L.G. Hou, J.S. Zhang, An improved thermos-mechanical treatment of high-strength Al-Zn-Mg-Cu alloy for effective grain refinement and ductility modification, J. Mater. Process. Technol. 239 (2017) 303–314.
[3] Y. Wang, G. Zhao, X. Xu, X. Chen, W. Zhang, Microstructures and mechanical properties of spray deposited 2195 Al-Cu-Li alloy through thermos-mechanical processing, Mater. Sci. Eng. A 727 (2018) 78–89.
[4] M.R. Barnett, F. Montheillet, The generation of new high-angle boundaries in aluminum during hot torsion, Acta Mater. 50 (2002) 2285–2296.
[5] W.C. Liu, J.G. Morris, Effect of hot and cold deformation on the β fiber rolling texture in continuous cast AA5052 aluminum alloy, Scr. Mater. 52 (2005) 1317–1321.
[6] F. Goli, R. Jamaati, Asymmetric cross rolling (ACR): a novel technique for enhancement of Goss/Brass texture ratio in Al-Cu-Mg alloy, Mater. Charact. 142 (2018) 352–364.
[7] C.D. Barrett, A. Imandoust, A.L. Oppedal, K. Inal, M.A. Tschopp, H.E. Kadiri, Effect of grain boundaries on texture formation during dynamic recrystallization of magnesium alloys, Acta Mater. 128 (2017) 270–283.
[8] A.S. Kumar, P.R. Dawson, Dynamics of texture evolution in face-centered cubic polycrystals, J. Mech. Phys. Solids. 57 (2009) 422–445.
[9] L. Donati, A. Segatori, M.E. Mehtedi, L. Tomesani, Grain evolution analysis and experimental validation in the extrusion of 6xxx alloys by use of a Lagrangian FE code, Inter. J. Plast. 46 (2013) 70–81.
[10] W.W. Zhou, S. Bang, H. Kurita, T. Miyazaki, Y.C. Fan, A. Kawasaki, Interface and interfacial reactions in multi-walled carbon nanotube-reinforced aluminum matrix composites, Carbon 96 (2015) 919–928.
[11] A. Bois-Brochu, C. Biais, F.A.T. Goma, D. Larouche, J. Boselli, M. Brochu, Characterization of Al-Li 2099 extrusions and the influence of fiber texture on the anisotropy of static mechanical properties, Mater. Sci. Eng. A 597 (2014) 62–69.
[12] A. Guzei, A. Jager, F. Parvizian, H.G. Lambers, A.E. Tekkaya, B. Svendsen, H.J. Maier, A new method for determining dynamic grain structure evolution during hot extrusion, J. Mater. Process. Technol. 212 (2012) 323–330.
[13] Z.C. Sun, L.S. Zheng, H. Yang, Softening mechanism and microstructure evolution of as-extruded 7075 aluminum alloy during hot deformation, Mater. Charact. 90 (2014) 71–80.
[14] M.G. Jiang, C. Xu, H. Yan, G.H. Fan, T. Nakata, C.S. Lao, R.S. Chen, S. Kamado, E.H. Han, B.H. Lu, Unveiling the formation of basal texture variations based on twining and dynamic recrystallization in AZ31 magnesium alloy during extrusion, Acta Mater. 157 (2018) 53–71.
[15] F.J. Humphreys, M. Hatherly, Recrystallization and Related Annealing Phenomena, second edition, (2004) New York.
[16] T.R. McNelley, S. Swaminathan, J.Q. Su, Recrystallization mechanisms during friction stir welding/processing of aluminum alloys, Scr. Mater. 58 (2008) 349–354.
[17] C. Schafer, J. Song, G. Gottstein, Modeling of texture evolution in the deformation zone of second-phases particles, Acta Mater. 57 (2009) 1026–1034.
[18] J.D. Robson, D.T. Henry, B. Davis, Particle effects on recrystallization in magnesium-manganese alloys: Particle-stimulated nucleation, Acta Mater. 57 (2009) 2739–2747.
[19] I.A. Ovidko, A.G. Sheinerman, Grain boundary sliding, triple junction disclinations and strain hardening in ultrafine-grained and nanocrystalline metals, Inter. J. Plast. 96 (2017) 227–241.
[20] K. Edalati, T. Masuda, M. Arita, M. Furui, X. Sauvage, Z. Horita, R.Z. Valiev, Room-temperature superplasticity in an ultrafine-grained magnesium alloy, Sci. Rep. (2017) 1–9.
[21] N. Fakhar, F. Fereshteh-Saniee, R. Mahmudi, High strain-rate superplasticity of fine- and ultrafine-grained AA5083 aluminum alloy at intermediate temperatures, Mater. Des. 85 (2015) 342–348.
[22] A. Hadadzadeh, F. Mokdad, M.A. Wells, D.L. Che, A new grain orientation spread approach to analyze the dynamic recrystallization behavior of a cast-homogenized Mg-Zn-Zr alloy using electron backscattered diffraction, Mater. Sci. Eng. A 709 (2018) 285–289.
[23] S.K. Pradhan, S. Mandal, C.N. Athreya, K.A. Babu, B. De Boer, V.S. Sarma, Influence of processing parameters on dynamic recrystallization and the associated annealing twin boundary evolution in a nickel base superalloy, Mater. Sci. Eng. A 17 (2017) 49–58.
[24] C.H. Fan, Y.B. Zhang, J.H. Driver, D.J. Jensen, Oriented growth during recrystallization revisited in three dimensions, Scr. Mater. 72 (2014) 9–12.
[25] Y. Fukuda, K. Oh-Ishi, M. Furukawa, Z. Horita, T.G. Longdon, The application of equal-channel angular pressing to an aluminum single crystal, Acta Mater. 52 (2004) 1387–1395.
[26] M.M. Miszczyk, H. Paul, J.H. Driver, P. Drzymala, Recrystallization nucleation in stable aluminum-base single crystals: crystallography and mechanisms, Acta Mater. 125 (2017) 109–124.
[27] F.J. Humphreys, P.N. Kalu, Dislocation-particle interactions during high temperature deformation of two-phase aluminum alloys, Acta Metal 35 (1987) 2815–2829.
[28] K. Huang, K. Marthinsen, Q.L. Zhao, R.E. Loge, The double-edge effect second-phase particles on the recrystallization behavior and associated mechanical properties of metallic materials, Prog. Mater. Sci. 92 (2018) 284–359.
[29] Y. Tang, Z. Chen, A. Borbely, G. Ji, S.Y. Zhong, D. Schryvers, V. Ji, H.W. Wang, Quantitative study of particle size distribution in an in-situ grown Al–TiB_2 composite by synchrotron X-ray diffraction and electron microscopy, Mater. Charact. 102 (2015) 131–136.
[30] Y.H. Zhang, D.J. Jensen, Y.B. Zhang, F.X. Lin, Z.Q. Zhang, Q. Liu, Three-dimensional investigation of recrystallization nucleation in a particle-containing Al alloy, Scr. Mater. 67 (2012) 320–323.
[31] T. Mayama, M. Noda, R. Chiba, M. Kuroda, Crystal plasticity analysis of texture

development in magnesium alloy during extrusion, Int. J. Plast. 27 (2011) 1916–1935.
[32] A. Staroselsky, L. Anand, A constitutive model for hcp materials deforming by slip and twining: application to magnesium alloy AZ31B, Int. J. Plast. 9 (2003) 1843–1864.
[33] M. Yamasaki, K. Hagihara, S. Inoue, J.P. Hadorn, Y. Kawamura, Crystallographic classification of kink bands in an extruded Mg–Zn–Y alloy using intragranular misorientation axis analysis, Acta Mater. 61 (2013) 2065–2076.
[34] R. Quey, R.R. Dawson, J.H. Driver, Grain orientation fragmentation in hot-deformed aluminum: experiment and simulation, J. Mech. Phys. Solids. 60 (2012) 509–524.
[35] A. Godfrey, D.J. Jensen, N. Hansen, Slip pattern, microstructure and local crystallography in an aluminum single crystal of brass orientation {110} < 112, Acta Mater. 46 (1998) 823–833.
[36] M. Arzaghi, B. Beausir, L.S. Toth, Contribution of non-octahedral slip to texture evolution of fcc polycrystals in simple shear, Acta Mater. 57 (2009) 2440–2453.
[37] A. Mecif, B. Bacroix, P. Franciosi, Temperature and orientation dependent plasticity features of Cu and Al single crystals under axial compression—I. lattice rotation effects and true hardening stages, Acta Mater. 45 (1997) 371–381.
[38] C.M. Cepeda-Jimenez, J.M. Garcia-Infanta, O.A. Ruano, F. Carreno, Achieving microstructures prone to superplastic deformation in an Al–Zn–Mg–Cu alloy by equal channel angular pressing, J. Alloys Comp. 546 (2013) 253–259.
[39] V.E. Panin, N.S. Elsukova, I.V. Vlasov, D.V. Borisyuk, Grain boundary sliding and rotational mechanisms of intragranular deformation at different creep stages of high-purity aluminum polycrystals at various temperatures and stresses, Mater. Sci. Eng. A 733 (2018) 276–284.
[40] T. Mungole, P. Kumar, M. Kawasaki, T.G. Longdon, The contribution of grain boundary sliding in tensile deformation of an ultrafine-grained aluminum alloy having high strength and high ductility, J. Mater. Sci. 50 (2015) 3549–3561.
[41] M.T. Perez-Prado, G. Gonzalez-Doncel, O.A. Ruano, T.R. Mcnelley, Texture analysis of the transition from slip to grain boundary sliding in a discontinuously recrystallized superplastic aluminum alloy, Acta Mater. 49 (2001) 2259–2268.
[42] R.S. Mishra, T.R. Bieler, A.K. Mukherjee, Superplasticity in powder metallurgy aluminum alloys and composites, Acta Metal. Mater. 43 (1995) 877–891.
[43] C.A. Stanford-Beale, T.W. Clyne, Extrusion and high-temperature deformation of fiber-reinforced aluminum, Comp. Sci. Technol. 35 (1989) 121–157.
[44] R. Ding, Z.X. Guo, Coupled quantitative simulation of microstructural evolution and plastic flow during dynamic recrystallization, Acta Mater. 49 (2001) 3163–3175.
[45] M.J. Luton, C.M. Sellars, Dynamic recrystallization in nickel and nickel-iron alloys during high temperature deformation, Acta Metall. 17 (1969) 1033–1043.
[46] H. Mirzadeh, A. Najafizadeh, Prediction of the critical conditions for initiation of dynamic recrystallization, Mater. Des. 31 (2010) 1174–1179.
[47] A. Momeni, K. Dehghani, G.R. Ebrahim, Modeling the initiation of dynamic recrystallization using a dynamic recovery model, J. Alloys. Comp. 509 (2011) 9387–9393.
[48] F.C. Salvado, F. Teixeira-Dias, S.M. Walley, L.J. Lea, J.B. Cardoso, A review on the strain rate dependency of the dynamic viscoplastic response of FCC metals, Pro. Mater. Sci. 88 (2017) 186–231.